ELSEVIER

Journal of Structural Geology 26 (2004) 1783–1801

JOURNAL OF STRUCTURAL GEOLOGY

www.elsevier.com/locate/jsg

Superheated friction-induced melts in zoned pseudotachylytes within the Adamello tonalites (Italian Southern Alps)

Giulio Di Toro[a], Giorgio Pennacchioni[a,b,*]

[a]Dipartimento di Geologia, Paleontologia e Geofisica, Università di Padova, Padova I-35137, Italy
[b]CNR Istituto di Geoscienze e Georisorse (Sezione di Padova), Padova, Italy

Received 28 April 2003; received in revised form 15 October 2003; accepted 20 January 2004

Abstract

Pseudotachylytes and cataclasites are present along a strike-slip fault zone in the tonalites of the Adamello intrusion (Italian Southern Alps). Ambient conditions during faulting were 0.25–0.3 GPa and 250–300 °C. Pseudotachylyte veins thicker than 6 mm are zoned and consist of two symmetric microlitic domains towards the vein walls and a central spherulitic domain. The thickness of the microlitic domains (x) increases linearly with the half total thickness (a) of the pseudotachylyte vein (commonly <2 cm) according to the relation: $x=(0.29\pm 0.12)a$. The spherulitic and microlitic domains have similar chemical composition but the microlitic domain has a lower amount of plagioclase clasts. A numerical model explains zoning as the result of the different cooling rates and clast/melt interactions at the center and periphery of thick veins. Zoning is compatible with the injection of a single pulse of superheated friction-induced melt ($T_{\mathrm{melt}}\cong 1450$ °C). Melt temperatures estimated by the clast/matrix ratio (O'Hara, 2001) are considerably lower (316–577 °C). It is suggested that the difference in the temperature estimates reflects a more complex slip history than a single seismic slip event along the fault during production of cataclasites/pseudotachylytes.

Keywords: Adamello batholith; Cataclasite; Pseudotachylyte; Earthquakes; Numerical modeling; Clast size distribution

1. Introduction

There is general agreement today that most pseudotachylytes are the product of wear, comminution and friction-induced melting during seismic slip along a fault (e.g. Spray, 1995; Ray, 1999; Wenk et al., 2000; O'Hara, 2001). Therefore, pseudotachylytes may be potentially used to constrain fault plane processes during an earthquake (Magloughlin and Spray, 1992).

In exhumed paleoseismic (i.e. pseudotachylyte-bearing) faults, the dynamic shear stress resistance achieved during slip along the fault plane may be calculated from the volume of friction-induced melt (Sibson, 1975), assuming that most of the mechanical work is converted to heat (e.g. Scholz, 1990). This would allow the comparison of single-jerk paleoseismic data from field studies with indirect seismological data from present-day earthquakes (Wenk et al., 2000). The calculation of shear stress from pseudotachylyte volumes requires an estimate of melt temperature (T_{melt}).

For tectonic pseudotachylytes, estimates of peak T_{melt} are in the range 750–1450 °C. Since friction-induced melts are produced by non-equilibrium melting on the whole rock scale (Spray, 1992), melt temperatures were calculated by SiO_2 glass composition ($T_{\mathrm{melt}}\geq 1450$ °C; Lin, 1994a), by microlite mineralogy ($T_{\mathrm{melt}}=890$–1100 °C: two pyroxene geothermometer (Toyoshima, 1990); $T_{\mathrm{melt}}=790$–820 °C: omphacite–garnet geothermometer (Austrheim and Boundy, 1994); $T_{\mathrm{melt}}>1000$ °C: pigeonite crystallization (Camacho et al., 1995)) and by the mineralogy of survivor clasts ($T_{\mathrm{melt}}\geq 1000$ °C; Maddock, 1983). In experimentally generated pseudotachylytes, the measured T_{melt} were 1100–1550 °C (Lin and Shimamoto, 1998). Recently, O'Hara (2001) has suggested the use of the volume ratio between lithic clasts and matrix in pseudotachylytes for estimating the friction-induced melt (or host rock) temperature.

Tectonic pseudotachylyte veins decorate fault planes discontinuously and their thickness typically ranges from millimeters to a few centimeters. As a consequence, melt lifetime is commonly in the range of a few to hundreds of

---

* Corresponding author. Correspondence address: Dipartimento di Geologia, Paleontologia e Geofisica, Università di Padova, Padova I-35137, Italy. Tel.: +390-49-827-2053; fax: +390-49-827-2070.

E-mail address: giorgio.pennacchioni@unipd.it (G. Pennacchioni).

0191-8141/$ - see front matter © 2004 Elsevier Ltd. All rights reserved.
doi:10.1016/j.jsg.2004.03.001

seconds (Sibson, 1975), depending on the host rock temperature, initial T_{melt} and reservoir dimension. Thus, a reconstruction of the cooling history from pseudotachylyte textures may provide an estimate of the initial T_{melt}.

A textural/compositional zoning of pseudotachylyte veins is often reported in the literature (e.g. O'Hara and Sharp, 2001) and many zoned pseudotachylytes show a transition from a microlitic to a spherulitic texture towards the vein center (Macaudière et al., 1985; Lin, 1994b; Fabbri et al., 2000; Shimada et al., 2001). Zoning has been interpreted as the result of contrasting cooling rate and degree of undercooling in different positions of the pseudotachylyte vein (Macaudière et al., 1985; Lin, 1994b) or by cyclic pulses of heating, melting and crystallization during a single large earthquake (Warr et al., 2003). However, a quantitative analysis of the relationship between textural zoning and the cooling history of pseudotachylyte veins is still lacking.

This paper describes zoned pseudotachylyte fault veins along a strike-slip fault across the intrusive Adamello massif in the Italian Southern Alps. The cooling history of pseudotachylyte veins is modeled numerically by a finite difference method and, assuming that textural zoning of the pseudotachylytes is related to the contrasting cooling history at different positions in the veins as suggested by experimental observations, the microstructure is used to constrain the initial T_{melt}. The T_{melt} estimated in this way is compared with temperatures calculated with O'Hara's (2001) geothermometer; the contrasting results of the two methods are discussed in terms of the genesis of pseudotachylyte.

2. Geologic setting

Pseudotachylytes and cataclasites occur along the Gole Larghe–Val di Genova fault zone. The fault zone is an E–W-trending strike-slip fault which crosscuts the whole northern Adamello Tertiary batholith in the Italian Southern Alps and is a main branch of the Tonale line (Fig. 1).

The studied outcrop is located in the upper Val di Genova along a fault segment where pseudotachylytes are particularly frequent between fault rocks. The study area is at the front of the Lobbia glacier (N 46°10′–E 10°35′) and provides excellent glacier-polished exposures for structural analysis. In this area the study fault zone is about 550 m thick and consists of closely spaced (1–5 m), subparallel discrete horizons of concentrated cataclastic deformation, 5–50 cm thick, connected by an anastomosing network of millimeter-to-centimeter thick cataclasites. Single faults may record displacements up to several meters (Di Toro, 2003).

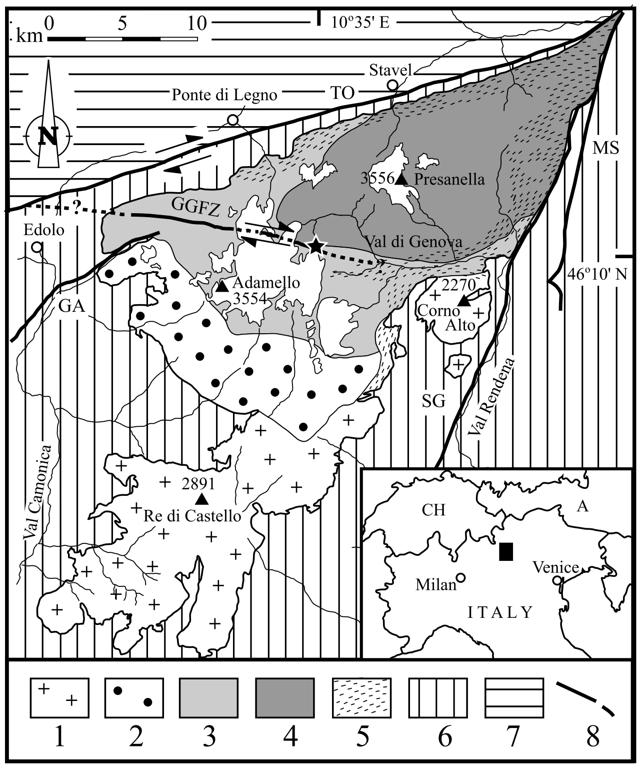

Fig. 1. Geological sketch map of the Adamello pluton (modified from Bianchi et al., 1970). Composite Adamello batholith: (1) Re di Castello body (42–40 Ma); (2) Western Adamello (36–34 Ma); (3) Central Peaks and Avio (34–32 Ma); (4) Presanella (33–29 Ma); (5) Foliated tonalites; (6) Southalpine basement and Permo-Mesozoic cover sequences; (7) Austroalpine nappes; and (8) main tectonic lines: GA = Gallinera; TO = Tonale; MS = Monte Sabion; SG = Southern Giudicarie; GGFZ = Gole Larghe–Val di Genova Fault Zone. Star along the GGFZ indicates the location of study pseudotachylytes. Location of the map (black box) is shown in the inset in the lower right corner of the figure.

The study fault zone cuts across hornblende-free, medium-grained tonalites belonging to the Avio intrusion (Bianchi et al., 1970) of the composite Adamello batholith. Biotite Rb–Sr and K–Ar radiometric cooling ages (34–32 Ma; Del Moro et al., 1983) are only slightly older than 30–27 Ma ages from zircon fission tracks (Viola, 2000). ^{40}Ar/^{39}Ar dating of three pseudotachylyte samples from the Lobbia outcrop gave a plateau age of 30 Ma (work in preparation: see communication in Müller et al. (2002)). The emplacement depth of the Adamello intrusion may be constrained by the mineral assemblages developed in the metamorphic contact aureole of the pluton (Werling, 1992; Stipp et al., 2002): pressures in the range of 0.25–0.3 GPa (corresponding to a depth of 9–11 km for a rock density of 2650 kg m^{-3}) may be inferred based on the absence of melting during the K-feldspar + sillimanite producing reaction and the observed polymorphic phase transformation of andalusite to sillimanite. Therefore fault exposures may be considered representative of relatively deep structural levels in the brittle domain.

3. Pseudotachylyte-bearing fault veins

3.1. Field observations

Pseudotachylytes occur typically in fault and injection vein associations (Fig. 2a and c) (Sibson, 1975) with different geometries, including single to paired generation surfaces (Grocott, 1981), side wall ripouts (Swanson, 1989) and pull-aparts with pseudotachylyte-welded breccia (Sibson, 1975). They are found both inside undeformed tonalites and precursor green, indurated cataclasites/ultracataclasites. The geometry of pseudotachylyte veins indicates the same kinematics as the associated cataclasites, and pseudotachylytes represent a late event of the brittle deformation, as they intrude cataclasites and only show minor and local reactivation by them. An intense fracture-related greenschist facies propylitic wall rock alteration (including chlorite–titanite after biotite, saussuritization of plagioclase and widespread epidote growth) is common in tonalite close to the cataclasite–pseudotachylyte horizons in part reflecting the damage zone around the cataclastic core zones of the faults. Epidote is pre- to post-kinematic to the deformation producing the cataclasites/pseudotachylytes.

Pseudotachylyte veins discontinuously decorate fault planes and usually are located at the cataclasite/tonalite boundary. The vein thickness is commonly less than 20 mm, but exceptionally thick veins may reach more than 100 mm and apparently represent dilational jogs (Scholz, 1990) along non-planar segments of fault planes. The contact of pseudotachylytes to tonalites or cataclasites is sharp.

On the basis of the internal structure three types of fault vein are distinguished: (i) unzoned, (ii) zoned, and (iii) convolute. The different types may occur together along the same fault vein and were observed inside both undeformed tonalites and cataclasites.

Unzoned fault veins are generally less than ~6 mm thick and have a homogeneous black color. Zoned fault veins include two symmetric outer black layers, similar in aspect to unzoned fault veins, sandwiching a central, lighter-colored layer. The contact between layers is usually sharp and zoning is easily identified in the field (Fig. 2b). A similar zoning is also observed in injection veins (Fig. 2c). Convolute fault veins show a distorted internal layering, often defining eye-shaped flow folds (e.g. Berlenbach and Roering, 1992), and are usually adjacent to vein-wall irregularities or to injection veins. Convolute fault veins are not treated further in this paper.

The thicknesses of the zoned fault veins and of the internal layers were measured on sections orthogonal to the veins both in outcrop and in thin section (Fig. 3). The thickness x of the outer black bands (corresponding to microlitic domains: see later) is similar and increases linearly with the half thickness (a) of the entire vein according to the relation:

$$x = (0.29 \pm 0.12)a \qquad (1)$$

for $a > 3$ mm

3.2. Microstructure

Optical microscopy and scanning electron microscopy (SEM) indicate that the external and internal layers of the zoned fault veins represent a microlitic domain and a spherulitic domain, respectively

(1) *Microlitic domain* consists of an intergrowth of randomly oriented microlites of plagioclase, with interstitial biotite and minor K-feldspar (Fig. 4a). Plagioclase microlites have abundant inclusions of biotite oriented parallel to plagioclase elongation (Fig. 4a–c). The width, length and morphology of plagioclase microlites vary across the microlitic domain. Dimensions of the microlites increase toward the spherulitic domain: in a 35-mm-thick vein, the maximum microlite width and length increases from less than 1 to 13 μm and from 1 to 280 μm, respectively.

From the host rock contact to the spherulitic domain, the morphology of plagioclase microlites changes from lath (Fig. 4a), often with paired crystals, to bow-tie and sheaf morphologies (Lofgren, 1971; Macaudière et al., 1985; Lin, 1994b) (Fig. 4b). Close to the spherulitic domain, several microlites associate in stellar aggregates or develop 'spherulitic' aggregates overgrowing plagioclase clast nuclei (Lofgren, 1974; Shimada et al., 2001) (Fig. 4c).

The microlitic domains commonly include angular lithic clasts of quartz and plagioclase (Fig. 4c) as well as of cataclasite (possibly some fine grained lithic clasts may represent former pseudotachylyte) and epidote veins; K-feldspar and biotite clasts are rare. Plagioclase microlites do not show any geometric relationship with quartz clasts (Fig. 4c).

The transition between the microlitic domain and spherulitic domain is either sharp, marked by a 40–100-μm-thick K-feldspar cryptocrystalline layer (Fig. 4d), or gradual.

(2) *Spherulitic domain* is a matrix-supported domain including spherulites, titanite grains, minor plagioclase microlites and relatively rounded lithic clasts (Fig. 4d–f). Under the optical microscope, the matrix is colorless to yellow pleochroic (more common) and shows homogenous extinction parallel to the vein boundary. Scanning and transmission electron microscopy (TEM) revealed that the matrix is microcrystalline K-feldspar (colorless matrix) or a cryptocrystalline polymineralic aggregate (yellow matrix) with both granular and oriented acicular microlites 0.1–0.4 μm long (Fig. 4e, g and h).

The spherulitic domain contains different types of spherulites whose characteristics are determined by the composition of the overgrown nuclei:

(i) Plagioclase-nucleus spherulites: plagioclase clasts are always surrounded by a composite shell including an inner rim of radially-arranged plagioclase microlites and an outer rim of mainly K-feldspar (Fig. 4e). When the nucleus of the spherulite is a polycrystalline plagioclase-quartz clast, the overgrowth of plagioclase microlites is only developed in contact with the plagioclase clast (Fig. 4e). The external rim following the plagioclase spherulitic corona may show complex zoning, including thin concentric zones rich

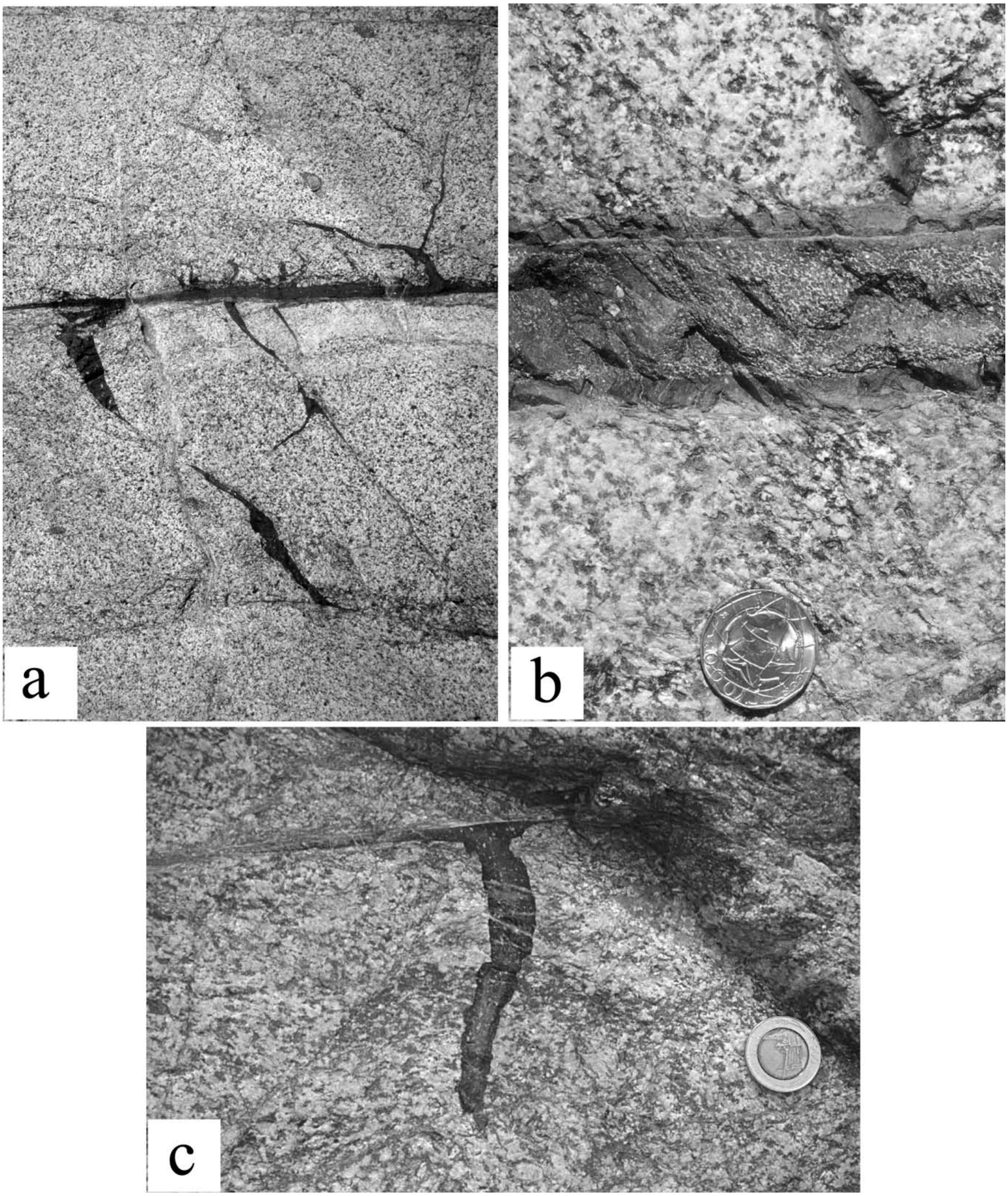

Fig. 2. (a) Pseudotachylyte fault and injection veins; the geometry of injection veins is consistent with dextral shear of a cataclastic precursor; (b) zoned fault vein with symmetric homogeneous outer black layers (microlitic domains) and a central lighter zone (spherulitic domain); and (c) zoned injection vein inside an altered and partly cataclastic tonalite. In all photos, coin (25 mm in diameter) for scale.

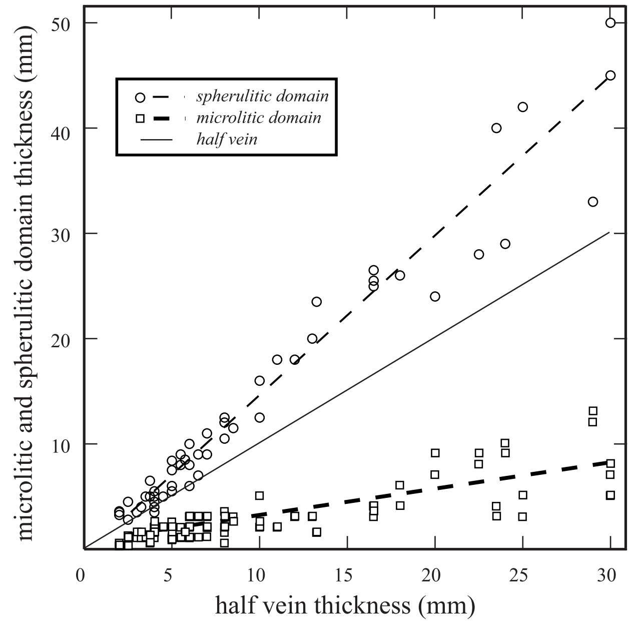

Fig. 3. Plot of thickness of the microlitic domain and spherulitic domain vs. the half total vein thickness.

in K-feldspar or silica, respectively (Fig. 4f). The plagioclase microlites of the plagioclase-nucleus spherulites have similar characteristics as the ones in the microlitic domain, with fine coaxial interleaving of biotite and an external rim of biotite (Fig. 4e and f).

(ii) Quartz-nucleus spherulites: quartz clasts are commonly rounded to elliptical in shape (aspect ratio <1.5) and show a spherulitic overgrowth composed of a biotite-rich inner zone grading to an outer rim of dominantly silica (Fig. 4e–g). In samples with flow structure in the matrix (Fig. 4g), quartz-nucleus spherulites are elongated with the long axis parallel to the flow direction and have silica-rich tails (Fig. 4g).

As in the plagioclase-nucleus spherulites, individual microlites scattered in the spherulitic domain have an external rim of microcrystalline K-feldspar and cryptocrystalline silica (Fig. 4h).

Rounded poikilitic (biotite inclusions) titanite grains are very common in the matrix of the spherulitic domain (Fig. 4e and f); under the TEM they appear as aggregates of submicron-sized granular titanite associated with minor interstitial biotite. The titanite grains decrease in grain size (ranging in diameter from a few microns to 50 μm) and increase in number towards the vein center. Titanite grains were never observed inside the plagioclase spherulitic rim of the plagioclase-nucleus spherulites, but are included in the outer K-feldspar layer (Fig. 4e and f). Titanite grains are also external to the quartz-nucleus spherulites (or rarely included in the outer silica-rich rim (Fig. 4f)).

Fe-rich epidote crystals, which commonly overgrow magmatic allanite clasts, are relatively frequent in the spherulitic domain. Epidote overgrows the titanite grains and locally invades the external rim of the plagioclase-nucleus spherulites and quartz-nucleus spherulites (Fig. 4f and g). Apatites often have, similarly to epidote crystals, a rounded nucleus and a dendritic outer shell.

Biotite is not present as clasts in the spherulitic domain. Compared with lithic clasts in the microlitic domain, plagioclase clasts are rounded and quartz clasts commonly show straight fractures and rectilinear outer borders. Cataclasite clasts have deep embayments filled by acicular biotite and minor K-feldspar and smaller clasts, mainly of quartz, are aligned and connected at larger cataclasites clasts.

Amygdules and vesicles, which are considered typical of pseudotachylytes produced at shallow levels (e.g. Maddock et al., 1987; Magloughlin, 1998), have never been observed in either the spherulitic or the microlitic domain.

3.3. Image analysis

Image analysis was performed on both microlitic and spherulitic domains to estimate: (i) the clast/matrix ratio, (ii) the cumulative clast size distribution (CSD), (iii) the percentages of plagioclase and quartz between clasts, and (iv) the plagioclase/biotite ratio between microlites Image analysis data are reported in Table 1. Image analysis was carried out with NIH-Image software (http://rsb/info.nih.gov/nih-image/) on both optical microscope and SEM (back-scattered electron, BSE) images of polished thin sections at magnifications in the range 50–1500×. Optical microscope images were digitally imported using a video camera connected to a microscope.

Under the optical microscope the light color of the feldspar and quartz clasts compared with the matrix/microlites allowed the clast/matrix ratio to be estimated automatically using a grayscale range select option in the Image software. A test of the reliability of clast/matrix data collected in this way was made on several thin sections by comparing the clast/matrix ratio determined automatically by grayscale thresholding on both SEM and optical images with that determined by outlining the clasts by hand on the same images. Measured clast/matrix values are in the range 0.1–0.2 and differences between automatically and manually determined values are less than 1%. In SEM images, quartz clasts were outlined automatically and plagioclase clasts were outlined manually (since they have the same grayscale tone as the microlites). For the CSD, owing to the presence of polymineralic clasts, it was necessary to manually outline the clasts.

Most of the clast/matrix data were collected from mosaics of SEM images (each of area 5.6 mm^2) at 50× magnification and 3 μm resolution to allow a meaningful area to be analyzed (Ray, 1999; O'Hara, 2001): this means that clasts less than 10 μm^2 in area were not counted. However, the CSD plot (Fig. 5, filled squares) indicates that the contribution of small clasts (i.e. clast size <200–300 μm^2) to the total clast area is negligible. In high

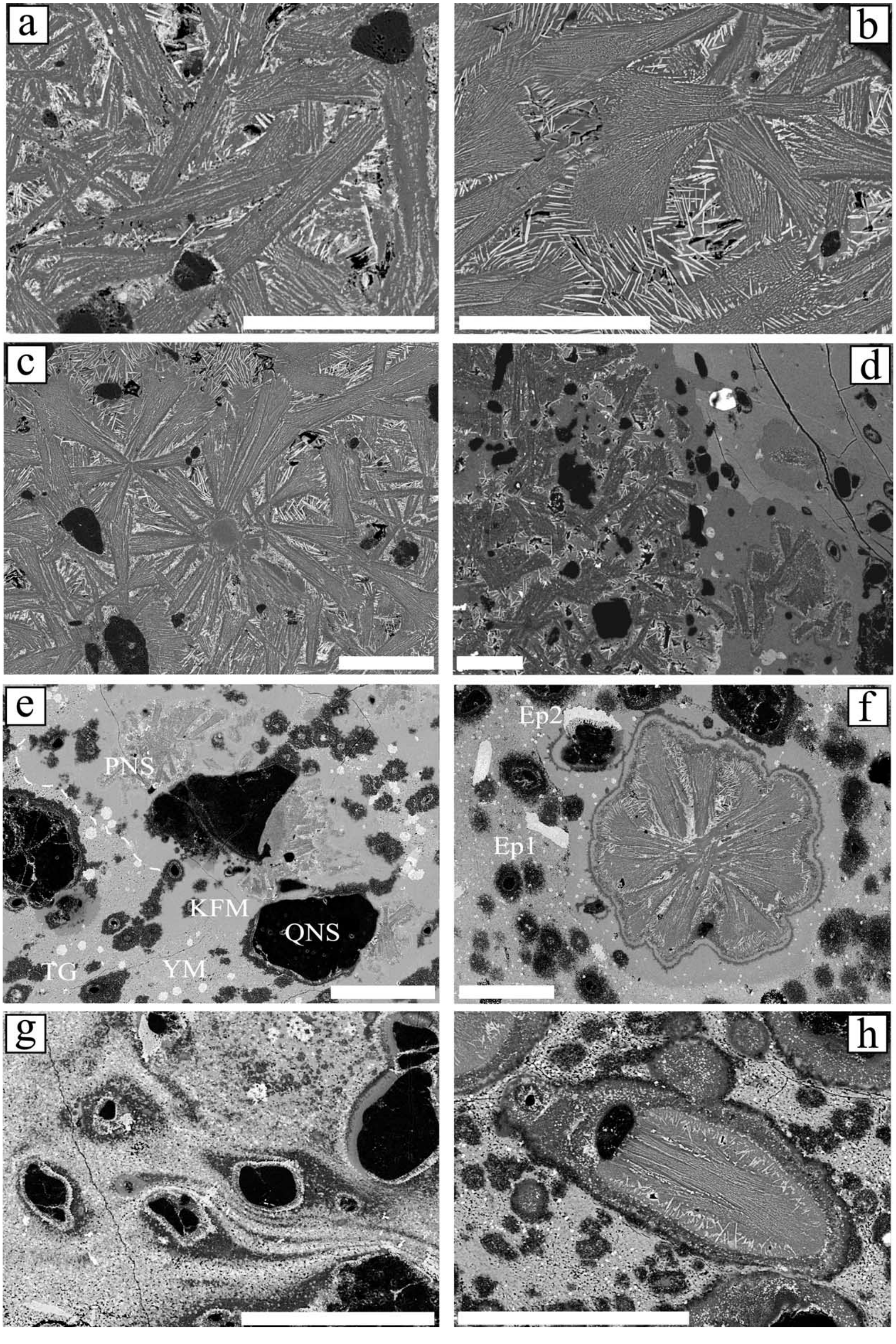
a
b
c
d
e
PNS
KFM
QNS
TG
YM
f
Ep2
Ep1
g
h

Table 1
Image analysis data of the study pseudotachylytes. The last column of the table reports T_{melt} values estimated with Eq. (8) of O'Hara (2001) and assumed a $T_{hr} = 250$ °C. UFV = unzoned fault vein; ZFV = zoned fault vein; MD = microlitic domain; SD = spherulitic domain; VLM = visible light microscope; bt = biotite; pl = plagioclase; qtz = quartz; $2a$ = thickness of the pseudotachylyte vein

Sample	Domain	Image	Areas		% Clasts				% Miner. between clasts				% bt in MD		$2a$	T_{melt}
			#	mm^2	Automatic	s.d.	Manual	s.d	% qtz	s.d.	% pl	s.d.	% bt	s.d.	mm	°C
A2 1	UFV MD	SEM BSE	2	8.34			20.5	0.3	11.4	0.7	9.1	1.0	26.4		2	431
A2	UFV MD	VLM	11	57.04	21.6	2.3									2	449
24-00	UFV MD	SEM BSE	1	5.02			12.8								4	340
32-00	ZFV MD	VLM	3	17.13	14.4	0.9							27.3-17.2		13	356
11-00HD	ZFV MD	SEM BSE	6	4.90			27.8	5.6	14.3	1.5	14.9	3.7	31.6		15	577
11-00LD	ZFV MD	SEM BSE	19	9.60			20.0	1.0	12.1	4.2	8.4	0.9	29.2-38.2		15	424
Ad46b	ZFV MD	SEM BSE	4	6.24			21.8	3.2	12.7	3.0	9.1	2.4	24.3	2.4	17	452
Ad46b	ZFV MD	VLM	11	30.33	15.9	4.9									17	372
20-00a	ZFV MD	SEM BSE	2	9.85			13.3	0.2	10.7	1.2	2.6	1.1	21.1	0.6	35	345
20-00b	ZFV MD	VLM	3	26.81	15.8	2.8	16.8	4.2							35	370-382
20-00c	ZFV MD	SEM BSE	1	5.49			13.5								35	346
20-00c	ZFV MD	VLM	1	5.49	13.4		14.5								35	345-357
01-00	ZFV MD	VLM	1	3.37	12.5								15.3		50	337
11-00HD	ZFV SD	SEM BSE	1	2.67			14.6		13.3		1.3				15	358
11-00LD	ZFV SD	SEM BSE	4	9.74			16.7	1.7	11.3	0.1	5.4	1.6			15	381
Ad46b	ZFV SD	SEM BSE	7	7.99			11.5	1.5	10.0	1.3	1.6	0.6			17	328
20-00	ZFV SD	SEM BSE	2	16.58			10.1	0.5	9.2	0.4	0.9	0.2			35	316
20-00	ZFV SD	VLM	2	30.23			10.8	2.0							35	322
01-00	ZFV SD	VLM	3	40.52	11.1	3.4							18.8		50	325

magnification images (500 × magnification, 0.3 μm resolution, which is the mean grainsize of the cryptocrystalline 'yellow matrix'), a similar shape of the clast size vs. total clast area curve is obtained (Fig. 5, empty squares), but the curve is shifted toward smaller grain-sizes. The 500 × magnification was selected because TEM investigation showed that clasts in the spherulitic domain were larger than 1.5 μm in diameter. Data from 500 × images cannot be taken as representative given the small size of the area investigated. However, even in this case, the contribution of clasts with dimensions <50 μm^2 to the total clast area is less than 10%.

An advantage of using SEM images for clast analysis is the possibility of determining the contributions of quartz and plagioclase to the total clast area. Fig. 6a–c shows the distribution of quartz and plagioclase clasts across three zoned fault veins of different thickness. For the analysis, we used mosaics of SEM images, covering the entire (samples 11-00 and Ad46b; Fig. 6a and b) or one-third (sample 20-00; Fig. 6c) of the vein thickness. In general, the total clast content is slightly higher in the microlitic domain (25–15% and up to 28% in an anomalous clast-rich layer of sample 11-00) than in spherulitic domain (20–10%). In both samples 11-00 and Ad46b, clasts of the spherulitic domain concentrate slightly towards the vein interior. In the spherulitic domain, the decrease (compared with the microlitic domain) in total clasts is related to the disappearance of plagioclase (11-00, 20-00) or to consumption of both quartz and plagioclase (Ad46b). The plot of mean clast area vs. total vein thickness (Fig. 7) shows a nearly linear decrease in clast content with increasing fault vein thickness in both the microlitic and spherulitic domain, and a more pronounced decrease of plagioclase compared with quartz.

In the microlitic domain, the ratio of biotite to plagioclase microlites was determined via image analysis

Fig. 4. Microstructures in the microlitic domain ((a)–(d)) and spherulitic domain ((d)–(h)) inside zoned fault vein. Microlitic domain: (a) randomly oriented plagioclase 'rod' microlites (medium gray) with fine inclusions of biotite (white) and interstitial acicular biotite. The small plagioclase microlites at the left side form the chilled margin. Quartz clasts are black. Center of the image is 3.4 mm from the host rock. (b) Bow-tie and sheaf-shaped plagioclase microlites. Center of the image is 4.3 mm from the host rock. (c) Stellar spherulite made of plagioclase microlites radiating from a plagioclase clast nucleus (medium gray). Center of the image is 4.5 mm from the host rock. Boundary between microlitic domain and spherulitic domain: (d) sharp contact between the microlitic and spherulitic domain marked by a 40–100-μm-thick K-feldspar layer (medium gray). Spherulitic domain: (e) microlites of plagioclase rim plagioclase clasts and form plagioclase-nucleus spherulites (PNS), whereas quartz clasts are rimmed by a thin layer of biotite and silica and form quartz-nucleus spherulites (QNS). Bright spots are rounded titanite grains (TG) locally included in the external layer of spherulites. The matrix consists of a homogeneous medium gray K-feldspar matrix (KFM) and a cryptocrystalline (grain size of 0.1–0.4 μm) polymineralic matrix (yellow matrix in thin section, YM) of biotite + feldspar. The dashed line outlines the contact between the yellow matrix and the K-feldspar matrix. (f) Complex plagioclase-nucleus spherulites with a double cryptocrystalline external layer made of K-feldspar (medium gray) and silica (dark gray). Idiomorphic epidote (Ep1) has a Ce-rich nucleus (allanite) and a Fe-rich external rim. Non-idiomorphic epidote (Ep2) overgrows the external layer of quartz-nucleus spherulites and includes titanite grains. (g) Quartz clasts develop silica rich tails and flow structures. (h) Plagioclase microlites in the spherulitic domain with external K-feldspar (medium gray) and silica (black) rich layers. All photos are SEM–BSE images with scale bar 100 μm long.

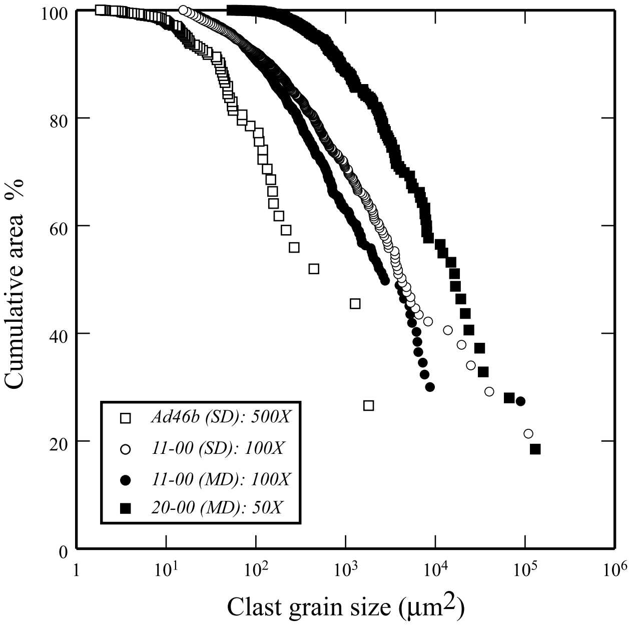

Fig. 5. Cumulative clast size distribution of lithic clasts from SEM–BSE images taken at 500 × (empty squares: spherulitic domain (SD) of sample Ad46b; resolution 0.3 µm), 100 × (filled and empty circles: microlitic domain (MD) and spherulitic domain (SD), respectively, of sample 11-00; resolution 1.5 µm) and 50 × (filled squares: microlitic domain (MD) of sample 20-00; resolution 3 µm). See text for explanation.

of SEM micrographs (500 × magnification, 0.156 mm^2 inspected area) using the good grayscale contrast between the two minerals. Acicular biotite usually comprises about 20% of the matrix in the microlitic domain; however, some enrichment in biotite was observed (i) near the host rock contact, (ii) in unzoned fault veins or thin (< 10 mm) zoned fault veins, and (iii) locally in microlitic domains of zoned fault veins.

3.4. Geochemistry and microchemistry

3.4.1. X-ray fluorescence

X-ray fluorescence analysis of unzoned fault veins (two samples), zoned fault veins (three samples), cataclasites (four samples) and host rock (four samples) are reported in Table 2. In the zoned fault vein, the composition of the bulk vein and, for sample 20-00, separately the microlitic and spherulitic domains, were determined. The matrix composition was calculated by subtracting the compositions of the quartz and feldspar clasts, weighted by the volumes of these minerals determined from image analysis, from the bulk composition of the pseudotachylyte. The composition of plagioclase clasts was determined by electron microprobe.

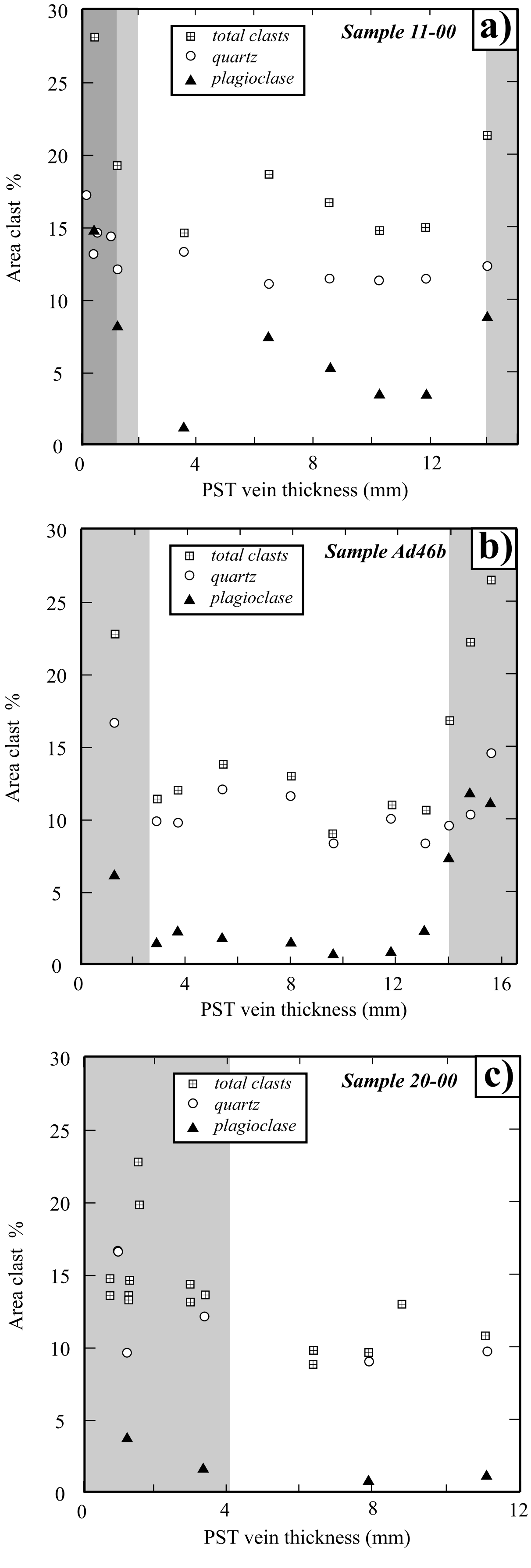

Fig. 6. Clast (area) percentage as a function of position in different zoned fault vein. The two lateral medium gray bands are the microlitic domain. (a) Zoned fault vein, 11-00, total vein thickness 15 mm. In dark gray, zone of the microlitic domain with exceptionally high clast content; (b) zoned fault vein, Ad46b, total vein thickness 16.5 mm; (c) zoned fault vein, 20-00, total vein thickness 35 mm (only one third of vein shown).

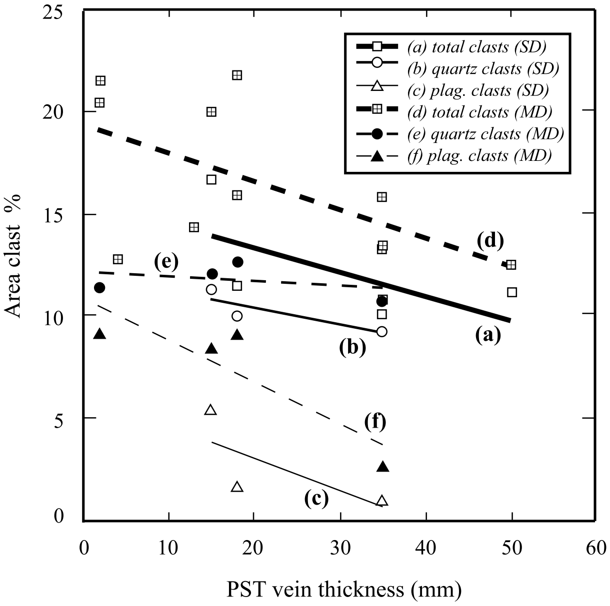

Fig. 7. 2D mean clast content (expressed as area percentage) vs. thickness of fault veins for nine different samples (SD = Spherulitic domain; MD = Microlitic domain). See text for description.

The compositions of the pseudotachylytes are quite similar to each other and comparable with those of the cataclasites. The pseudotachylytes and cataclasites are enriched in K_2O, Lost On Ignition (L.O.I.) and FeO_{tot} and depleted in SiO_2, CaO and Na_2O with respect to the tonalite host rock (Table 2). In sample 20-00, the microlitic and spherulitic domains are of similar composition.

3.4.2. Electron microprobe

Mean electron microprobe compositions are reported in Table 3 for: (i) feldspar and biotite of the host rock, (ii) matrix and microlites (plagioclase and titanite) in pseudotachylyte veins. The composition of microlitic plagioclase is always contaminated by the biotite, present as ubiquitous fine interleaving, and microprobe analyses with the lowest K, Ti, Fe and Mg content were selected. Microlitic plagioclase in the zoned fault veins has An_{40} composition identical to that of large plagioclase microlites, nearly free of biotite inclusions, present in injection veins.

Based on XRF bulk analyses and the microprobe compositions of minerals, the following modal composition of the host rock was calculated: 48% An_{45}-plagioclase, 29% quartz, 17% biotite and 6% K-feldspar and accessory zircon, apatite and titanite. This composition is perfectly consistent with the compositions reported in the literature for Avio tonalites by Bianchi et al. (1970) and with the optical observation under the microscope.

Assuming that the XRF composition of the pseudotachylyte matrix (Table 2) is the composition of the friction-induced melt, we determined its liquidus temperature with MELTS (http://www.washington.geol.edu). The estimated liquidus temperature was between 1050 and 1170 °C, depending on water content, depth of formation (see next paragraph) and water fugacity.

4. Host rock pressure–temperature conditions during faulting

Pressure and temperature (T_{hr}) of the host rock during formation of cataclasite/pseudotachylyte within fault zone may be constrained by different types of data: (i) the deformation mechanisms of quartz in the cataclasites synkinematic to pseudotachylyte formation; (ii) the mineral association of fracture-related wall rock alteration and associated veining coeval to cataclasite/pseudotachylyte, (iii) the absence of amygdules in pseudotachylytes (iv) geochronological data.

(i) In cataclasites, the deformation mechanism of quartz is dominantly fracturing. However, especially in relatively low-strain domains, some cataclasites show evidence for incipient recrystallization to very fine-grained (grain size <5 μm) aggregates of new quartz (quartz II), mainly localized in microcrack networks associated with a patchy extinction of quartz clasts (Fig. 8a). Microstructures are consistent with bulging recrystallization and/or fluid-assisted quartz precipitation along microcracks. TEM images of quartz II show locally high dislocation densities and commonly pervasive presence of small fluid inclusions (Fig. 8b). A ‘water-rich composition’ of quartz II is also indicated by its rapid decomposition under the TEM beam. Grain boundary porosity is present in the form of extensive fine pitting along the grain faces and fluid pockets occur at triple-grain junctions with cross-sectional geometry, characterized by wetting angles $<60°$, typical of water-rich fluids (Watson and Brenan, 1987) (Fig. 8b). Incipient crystal plasticity of quartz suggests a temperature close to 280–300 °C (Stipp et al., 2002).

(ii) Fracture-related greenschist facies propylitic alteration, associated with extensive epidote veining, is coeval to the cataclasite-pseudotachylyte deformation and suggests temperatures in the range 200–300 °C (e.g. Guilbert and Park, 1986).

(iii) The absence of vesicles/amygdules is typical of relatively deep-seated pseudotachylytes (e.g. Maddock et al., 1987; Killick and Roering, 1998; Magloughlin, 1998). An estimate of the ambient pressure can be made using the equimolal solubility model of Burnham (1979). In vesicle-free melts, the amount of dissolved water is a function of lithostatic pressure, T_{melt} and concentration of exchangeable cations (alkali metals, alkaline earths and transition metals). According to Burnham (1979), when the alkali/Al (cations) ratio is less than one, the number of exchangeable cations equals the number of moles of Al^{3+} (n_{Al}) and from n_{Al}

Table 2

Major element XRF composition of pseudotachylytes, cataclasites and host rock tonalites. In the case of pseudotachylytes, for each sample the table reports both the original XRF analysis (first column) and the analysis corrected for clast contribution (second column) based on the clast amount determined by image analysis: Ad50b(c) = Ad50b−(11% quartz + 9% plagioclase); 24-00(c) = 24-00−(11% quartz + 9% plagioclase); Ad46b(c) = Ad46b−(11% quartz + 4% plagioclase); 32-00(c) = 32-00−(10% quartz + 6% plagioclase); 20-00b(c) = 20-00b−(10% quartz + 2.6% plagioclase); 20-00b*(c) = 20-00b*−(10% quartz + 1.6% plagioclase). Vein thicknesses of pseudotachylytes are: Ad50b = 5 mm; 24-00 = 4 mm; Ad46b = 17 mm; 32-00 = 13 mm; 20-00b = 35 mm. UFV = unzoned fault vein; ZFV = zoned fault vein; MD = microlitic domain; SD = spherulitic domain; PST = pseudotachylyte

	UFV				ZFV				ZFV_MD		ZFV_SD		Host rock		PST bulk		PST bulk (c)		Cataclasite	
	Ad50b	Ad50b(c)	24-00	24-00(c)	Ad46b	Ad46b(c)	32-00	32-00(c)	20-00b	20-00b(c)	20-00b*	20-00b*(c)	4 data	s.d.	6 data	s.d.	6 data	s.d.	4 data	s.d.
SiO_2	60.80	56.38	63.89	60.08	59.69	55.05	61.78	58.00	62.95	58.99	64.42	61.08	66.40	0.87	62.26	1.67	58.26	2.07	63.15	1.17
TiO_2	0.70	0.88	0.53	0.66	0.55	0.65	0.55	0.67	0.54	0.63	0.53	0.59	0.46	0.05	0.57	0.06	0.68	0.09	0.48	0.04
Al_2O_3	16.93	18.28	16.57	17.76	17.13	19.03	17.06	18.39	17.00	18.93	16.68	18.24	16.59	0.35	16.89	0.20	18.44	0.43	16.70	0.70
FeO	2.92	3.66	3.19	3.99	3.09	3.65	3.50	4.23	3.74	4.34	3.19	3.59	3.44	0.29	3.27	0.27	3.91	0.29	3.23	0.28
Fe_2O_3	1.98	2.47	1.22	1.51	2.00	2.36	0.83	0.99	0.87	1.00	0.92	1.03	0.33	0.08	1.30	0.50	1.56	0.63	1.03	0.39
MnO	0.10	0.11	0.12	0.13	0.11	0.12	0.13	0.14	0.14	0.16	0.10	0.11	0.09	0.01	0.11	0.01	0.13	0.02	0.13	0.01
MgO	2.04	2.57	1.77	2.22	1.95	2.31	1.84	2.22	1.91	2.22	1.71	1.92	1.59	0.17	1.87	0.11	2.24	0.19	1.72	0.13
CaO	3.89	3.84	3.58	3.44	3.55	3.77	3.62	3.60	4.09	4.47	3.89	4.19	4.49	0.07	3.77	0.20	3.89	0.35	3.31	0.68
Na_2O	2.56	2.55	3.03	3.12	1.26	1.21	1.59	1.42	3.22	3.56	2.99	3.25	2.96	0.05	2.44	0.75	2.52	0.90	1.41	0.35
K_2O	4.41	5.50	3.15	3.90	5.92	6.99	5.02	6.04	2.98	3.44	2.83	3.18	2.17	0.09	4.05	1.16	4.84	1.42	6.86	0.41
P_2O_5	0.13	0.16	0.13	0.16	0.13	0.16	0.14	0.16	0.14	0.16	0.14	0.15	0.12	0.01	0.13	0.00	0.16	0.00	0.12	0.01
L.O.I.	2.86	3.60	2.41	3.03	3.96	4.69	3.40	4.12	1.81	2.10	2.36	2.66	0.91	0.06	2.80	0.71	3.37	0.88	1.73	0.07
Tot	99.31	100.00	99.58	100.00	99.34	100.00	99.45	100.00	99.39	100.00	99.74	100.00	99.55	0.13	99.47	0.15	100.00	0.00	99.87	0.38

Table 3

Microprobe compositions of lithic clasts (host rock minerals), microlites and matrix in pseudotachylytes

	Titanite grains		White matrix		Yellow matrix		Feldspar microlites		Plagioclase (clasts)		K-feldspar (clasts)		Host rock biotite	
	4 data	s.d.	9 data	s.d.	23 data	s.d.	7 data	s.d.	15 data	s.d.	6 data	s.d.	12 data	s.d.
SiO_2	34.31	1.10	64.28	0.51	43.69	0.51	58.16	1.22	56.20	1.28	63.53	0.73	35.45	0.19
TiO_2	22.12	2.30	0.05	0.07	0.42	0.06	0.12	0.03	0.02	0.01	0.22	0.22	2.55	0.50
Al_2O_3	13.04	2.18	18.66	0.22	24.69	0.95	25.26	0.73	26.96	0.94	18.58	0.28	17.33	0.20
FeOtot	1.74	0.50	0.33	0.14	9.91	1.41	1.10	0.36	0.38	0.29	0.43	0.16	20.59	0.42
MnO	0.07	0.03	0.02	0.04	0.21	0.07	0.05	0.05	0.12	0.11	0.05	0.03	0.01	0.01
MgO	0.56	0.14	0.08	0.06	4.35	0.49	0.43	0.16	0.02	0.01	0.69	0.31	9.04	0.46
CaO	23.37	0.62	0.31	0.18	0.84	0.27	8.19	0.55	9.33	1.02	0.13	0.23	0.03	0.04
Na_2O	0.27	0.39	0.58	0.16	0.05	0.03	5.87	0.44	5.98	0.62	1.12	0.49	0.08	0.02
K_2O	0.86	0.18	14.98	0.34	8.61	0.46	1.11	0.49	0.53	0.22	15.16	0.76	9.33	0.44
Tot	96.34	1.34	99.29	0.75	92.78	0.88	100.30	0.59	99.54	0.76	99.91	0.48	94.43	0.88

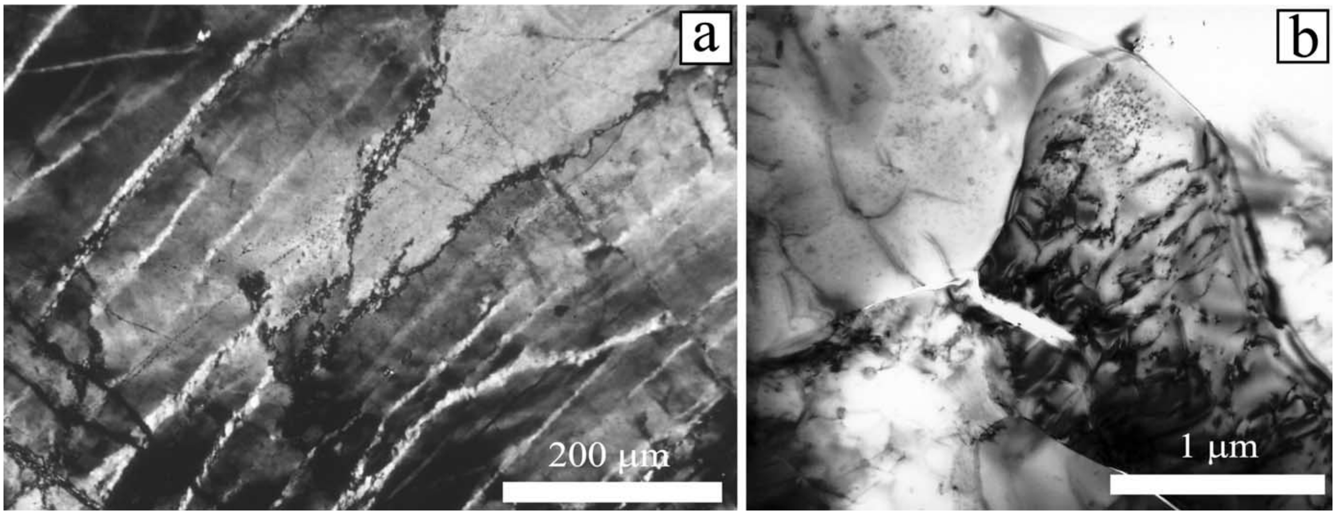

Fig. 8. Quartz microstructures in the host rock. (a) Optical microscope image of quartz grains in low strain domains, showing patchy extinction, deformation bands and fine aggregates of quartz II with microstructures consistent with recovery of dislocations by bulging recrystallization or precipitation from silica rich fluids; (b) TEM image of quartz II sampled in fractures kinematically consistent with pseudotachylytes and cataclasites. Grain faces are pitted by fluid inclusions (top center), and triple grain junctions have angles < 60° (top center). Quartz II (center) has a high density of dislocations and its upper corner is pitted by small dots (water bubbles). Quartz II (left) has few dislocations and a high density of bubbles.

it is possible to calculate the mole fraction of water X_m^w dissolved in a melt (Burnham, 1979, eq. 16-5). In sample Ad46b (having the highest L.O.I. between pseudotachylyte: 4.76%; Table 2), alkali/Al < 1, $n_{Al} = 0.38$ (for 100 g of rock) and $X_m^w = 0.42$. With these values, using the empirical plot of equimolal solubility vs. pressure (Burnham, 1979, fig. 16-4) and assuming a T_{melt} of 1100 °C (see MELTS liquidus temperature estimate) a pressure of 0.13 GPa (approximately 3.4 km depth for a rock density of 2650 kg m^{-3}) can be estimated. This estimate is slightly lower than the pressures ($P = 0.25$–0.30 GPa) inferred by Werling (1992) for contact metamorphism along the north-eastern border of the Adamello.

(iv) ^{40}Ar/^{39}Ar radiometric dating of pseudotachylytes yields an age of 29.8 ± 0.4 Ma (work in preparation: see communication in Müller et al. (2002)), which is also the intrusion age of the Presanella pluton adjacent to the Avio body (Del Moro et al., 1983) (Fig. 1). Along the northern border of Presanella contact metamorphism was coeval with dextral strike-slip deformation associated with the Tonale Line that produced mylonites to cataclasites along the temperature gradient of the contact aureole (Werling, 1992; Stipp et al., 2002). Therefore, deformation along the Gole Larghe–Val di Genova Fault Zone is likely synkinematic to the deformation along the Tonale Line; since there is no geological evidence for any later differential uplift of the Presanella relative to Avio and for any regional tilting of the Adamello intrusion, the ambient conditions of deformation along the northern periphery of the Presanella can be taken roughly as also representative of the studied pseudotachylytes (the pseudotachylytes are actually approximately 1 km higher than the contact aureole north of Presanella). Pressures of 0.25–0.3 GPa, corresponding to 9–11 km depth, were estimated in the northern contact aureole of the Presanella (Werling, 1992).

The above data support a relatively deep origin of pseudotachylytes, close to the brittle–ductile transition. Ambient conditions along the studied section of the fault zone may be assumed at $T_{hr} = 250$–300 °C and $P = 0.25$–0.3 GPa.

5. Modeling of fault vein cooling

The equation for heat diffusion in a solid describes the spatial variation of temperature T at each instant t (Fourier, 1822):

$$\frac{dT}{dt} = \kappa\nabla^2 T \tag{2}$$

where ∇^2 is the Laplacian operator and κ (m^2 s^{-1}) is the thermal diffusivity.

The one-dimensional analytical solution of Eq. (2) for a sheet dike intrusion (which approximates the geometry of pseudotachylyte fault veins) can be found in Carslaw and Jaeger (1959, p. 54): in a dike/vein of thickness $2a$, the temperature T after time t at a distance x from the vein center is:

$$T = \frac{1}{2}T_o\left\{\mathrm{erf}\left[0.5(a+x)/(\kappa t)^{0.5}\right] + \mathrm{erf}\left[0.5(a-x)/(\kappa t)^{0.5}\right]\right\} + T_{hr} \tag{3}$$

where erf is the error function, T_{hr} the initial host rock temperature and T_o the starting temperature of the melt exceeding T_{hr}.

The theoretical cooling curves for a tabular vein may show significant differences in cooling rates at different positions in the vein depending on T_o and $2a$. There is experimental evidence that a change in microlite morphology may be related mainly to differences in the cooling rate of the melt. An evolution from acicular to sheaf or stellar-shaped microlites (as observed away from vein wall in the microlitic domain of zoned fault veins) was observed by Lofgren (1974) in different experiments performed at increasing melt cooling rates. Sheaf and paired microlites were produced in cooling stepping experiments by Lesher et al. (1999) at cooling rates of ~1000 °C h^{-1}, and Lofgren (1974) obtained spherical or fan spherulites at higher cooling rates. In pseudotachylytes, microlites/spherulites clearly derive from primary crystallization of the friction melt and the microlitic domain has a similar chemical composition as the spherulitic domain; therefore, it is reasonable to assume that zoned fault veins may develop during vein cooling when comparatively higher cooling rates are set up at the vein center compared with the vein periphery during the cooling history. The origin of microlites from primary crystallization of a single pulse of friction-induced melt is also consistent with the observed increase of the thickness (data set of 55 different faults) of the microlitic domain with the increase of total vein thickness (Fig. 3). These observations rule out, for the study rocks, the other mechanism responsible for zoning in pseudotachylytes proposed in the literature, namely multiple pulses of melt during a single large earthquake (Warr et al., 2003).

Different (i.e. with a different initial T_{melt}) numerical models of cooling of a thick (>6 mm, the minimum thickness of the zoned fault veins) vein were run in order to obtain a contrast in cooling rate in the vein center and periphery which could explain the crystallization of microlites and spherulites and the distribution of survivor clasts.

5.1. The numerical model

A finite-difference numerical model of pseudotachylyte vein cooling was performed to include the latent heat of crystallization of microlites in the microlitic domain. An electronic spreadsheet (Fig. 9) was used following the method of Philpotts (1990, p. 83) and based on Crank and Nicholson (1947). In the spreadsheet each cell has an assigned characteristic ‘width’ δx, which depends on the thermal properties of the material, the latent heat produced during microlite crystallization and the assumed time increment δt according to the relation:

$$\delta x = \sqrt{\kappa \delta t} \qquad (4)$$

The model is one-dimensional along a profile orthogonal to the vein wall. The model is symmetric with a central vein of 24 mm and a total width of 204 mm. In the spreadsheet, the first row represents the distance x from the vein center, calculated at the cell centers, by summing the δx of the intervening cells. The second row represents the initial temperature distribution in the host rock-vein system with vein cells at 1450 °C and host rock cells at 250 °C (see later discussion). The other rows represent the thermal state after different time increments. In each cell, identified by the index m (row ID) and n (column ID), the temperature is calculated according to:

$$T_{m,n} = 0.25(T_{m,n-1} + T_{m-1,n-1} + T_{m-1,n+1} + T_{m,n+1}) \qquad (5)$$

except for all outer column cells where T is assumed constant and equal to the initial (ambient) host rock temperature. The number of cell subdivisions of the host rock-vein system, and therefore the points at a distance x where T is calculated, depends on the chosen δt and increases with decreasing time interval. In the present numerical model $\delta t = 0.5$ s.

5.2. Input parameters

(a) *Thermal properties*. The thermal properties of the host rock and melt used in the numerical models are reported in Table 4. The thermal properties of the host tonalite and of the crystallized microlitic domain were calculated from those of the mineral constituents based on their modal percentage in the rock from XRF compositions and image analysis. The thermal diffusivity for both the host rock and microlitic domain was set to 1.57×10^{-6}–1.60×10^{-6} m^2 s^{-1} in the temperature range 827–1027 °C (crystallization interval of plagioclase microlites), consistent with values for granitoid rocks (Clauser and Huenges, 1995). An intermediate value for the thermal diffusivity of the melt (0.72×10^{-6} m^2 s^{-1}) within the range reported in literature (0.26×10^{-6}–1.0×10^{-6} m^2 s^{-1}: e.g. Philpotts, 1990; Spera, 2000) was assumed.

(b) *Crystallization window for plagioclase*. In basaltic melts, plagioclase with An_{40} composition (similar to that of plagioclase microlites in zoned fault veins) crystallized at ~1080 °C, in experiments with 0.1 MPa pressure and 2000 °C h^{-1} cooling rate, and a linear decrease of the crystallization temperature with increasing cooling rate was observed (Lesher et al., 1999). Because of the higher cooling rates achieved in fault veins and the buffering effects of lithostatic pressure or heterogeneous nucleation, we can reasonably assume a temperature of ~1000 °C for plagioclase crystallization in pseudotachylytes. A crystallization window of about 200 °C (between 1000 and 800 °C) is assigned in the numerical model as is commonly assumed for magmatic systems (Cashman, 1993; Marsh, 2000).

(c) *Latent heat contribution*. The latent heat of crystallization ΔH in the microlitic domain can be included in the

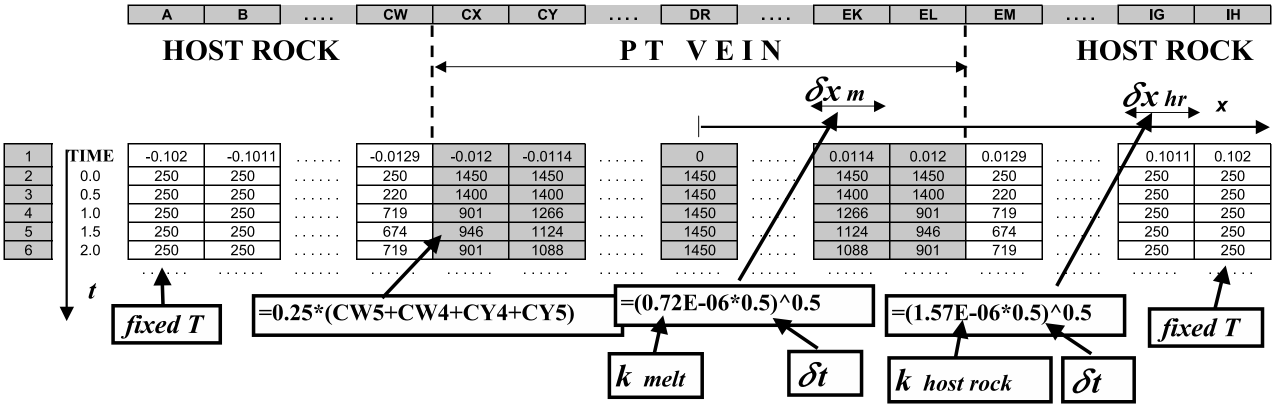

		A	B	....	CW	CX	CY	....	DR	....	EK	EL	EM	....	IG	IH
1	TIME	-0.102	-0.1011	......	-0.0129	-0.012	-0.0114	......	0	......	0.0114	0.012	0.0129	......	0.1011	0.102
2	0.0	250	250	......	250	1450	1450	......	1450	......	1450	1450	250	......	250	250
3	0.5	250	250	......	220	1400	1400	......	1450	......	1400	1400	220	......	250	250
4	1.0	250	250	......	719	901	1266	......	1450	......	1266	901	719	......	250	250
5	1.5	250	250	......	674	946	1124	......	1450	......	1124	946	674	......	250	250
6	2.0	250	250	......	719	901	1088	......	1450	......	1088	901	719	......	250	250

Fig. 9. An electronic spreadsheet created by following the method of Philpotts (1990, p. 83) and based on Crank and Nicholson (1947).

effective heat capacity c_p^* according to Spear (1995, p. 46):

$$c_p^* = c_p + \Delta H/\Delta T \tag{6}$$

where ΔT (200 °C) is the temperature interval of crystallization. In Eq. (6), ΔH is supposed to be exchanged uniformly during ΔT (Carslaw and Jaeger, 1959) and during the same ΔT since plagioclase and biotite crystallize almost altogether, as indicated by the ubiquitous fine interleaving of biotite inside plagioclase microlites (Fig. 4a–c). Since microlites (20% biotite and 80% plagioclase) comprise about 80% volume of the microlitic domain, the value for ΔH, is:

$$\Delta H = 0.8(0.80\Delta H_{\text{plagioclase}} + 0.20\Delta H_{\text{biotite}})$$
$$= 265 \text{ kJ kg}^{-1} \tag{7}$$

The effective heat diffusivity $\kappa^* = K/(\rho c_p^*)$ replaces κ in Eq. (4) in the microlitic domain, reducing the cell width when the latent heat of crystallization is released (Table 4).

Latent heat of crystallization is exchanged at the solid–liquid interface in the temperature range of crystallization. To include the contribution of the latent heat only from the areas of the fault vein that are crystallizing (i.e. at $1000 < T_{\text{melt}} < 800$ °C, see later discussion), fault vein cells were iteratively re-meshed when the temperatures fall inside the crystallization temperature range.

(d) *Initial and boundary conditions*. The initial and far field host rock temperature is set at 250 °C consistent with the inferred ambient temperature as discussed in Section 4. It is assumed that no significant heat is transferred to the country rock from fault surfaces during frictional sliding preceding pseudotachylyte generation, such that the ambient temperature close to the fault is not modified. This assumption is supported by the observation that zoning is also developed in thick injection veins (Fig. 2c) protruding far away from the generation surface and, therefore, where significant frictional heating may be excluded. Different experiments were run with different initial T_{melt} values in order to obtain contrasting cooling curves at the vein center and vein walls consistent with the textural zoning observed in the zoned fault vein.

(e) *No mass flux condition*. The duration of coseismic slip is in the range of few seconds (Swanson, 1992) and friction-induced melts are 'instantaneously' produced and injected in extensional jogs. Local flow structures (Fig. 4g) and clast concentration at the vein center (Fig. 6a and b), which may reflect the Bagnold effect during flow (Barrière, 1976), record melt motion. It is assumed that no significant flow follows this initial stage and, therefore, melt has an initial homogeneous temperature inside the vein. The random fabric of plagioclase microlites in the microlitic domain suggests static conditions during cooling/crystallization of the melt (Fig. 4a).

5.3. Results of the numerical model

In the case of a relatively thick vein (24 mm), an initial T_{melt} of ~1450 °C is required to set up a significant difference in cooling rates between the periphery and center of the pseudotachylyte vein. This cooling rate distribution inside the vein could explain (consistent with experimental data) the development of textural zoning in the pseudotachylytes. Fig. 10 shows the calculated cooling curves in the pseudotachylyte (i) at the vein/host rock contact, (ii) at 1.8 mm from the vein/host rock contact, and (iii) at the center of the vein. At the host rock contact (curve *a*), after an initial abrupt drop in T of about 650 °C in less than 10 s, the cooling rate remains relatively constant at 0.7 °C s^{-1}. In the microlitic domain (curve *b*) the temperature decreases ~1000 °C in 30–40 s and the cooling rate is 1.1 °C s^{-1} in the crystallization window. In the spherulitic domain (vein center, curve *c*) T_{melt} remains above the crystallization window for about 150 s and, when crystallization starts, the cooling rate is about 1.4 °C s^{-1}, i.e. approximately 25% higher than in the microlitic domain. An important consequence of the high initial T_{melt} is that cooling curves intersect the crystallization window after increasing time intervals starting from the wall toward the center of the vein (Fig. 10). Thus melt–clast interaction times do increase progressively toward the vein center, which determines a

Table 4

Thermal properties of the host rock, microlitic domain and melt used in the numeric model. The properties of the microlitic domain are for a composition of: 10% quartz clasts, 10% plagioclase clasts, 64% plagioclase microlites and 16% biotite microlites. Latent heat$_{MD}$ are thermal properties in the microlitic domain when heat is released due to crystallization of plagioclase (64%) and biotite (16%) microlites. Data on melting temperatures are from: Navrotsky (1995) (quartz, plagioclase, and K-feldspar), Spray (1992) (biotite) and Spera (2000) (granodiorite). c_p data (in the range 1100–1300 K) are from Holland and Powell (1990) (quartz, plagioclase, biotite and K-feldspar) and Spera (2000) (granodiorite wet at 1388 K and dry at 1600 K). ρ data are from Deer et al. (1992) (quartz, plagioclase, biotite and K-feldspar) and Spera (2000) (granodiorite). K data are from Clauser and Huenges (1995) (quartz, plagioclase, biotite and K-feldspar). κ values are calculated from $\kappa = K/(\rho c_p)$, with the exception of κ for the granodiorite/tonalite melt, which is set at an intermediate value within the range $0.26–1.0 \times 10^{-6}$ m^2 s^{-1} reported in the literature (e.g. Philpotts, 1990; Spera, 2000). ΔH values are from O'Hara (2001) (quartz, plagioclase, and K-feldspar) and Spera (2000) (granodiorite); the ΔH value for muscovite (O'Hara, 2001) is used for biotite

	% Mineral volume in the host tonalite	Melting T (K)	c_p (J kg^{-1} K^{-1})	ρ (kg m^{-3})	K (W m^{-1} K^{-1})	κ (10^{-6} m^2 s^{-1})	ΔH (kJ kg^{-1})	δx (10^{-4} m)
Quartz	0.29	1999	1186	2650	7.00	2.23	302	
Plagioclase	0.48	1830	1184	2650	5.50	1.75	302	
Biotite	0.17	930	1090	2950	1.00	0.31	453	
K-feldspar	0.06	1473	1153	2600	3.30	1.10	308	
Lobbia tonalite			1165	2709	4.97	1.60	332	9
Microlitic domain			1169	2693	4.93	1.57		9
Latent heat$_{MD}$			2493	2693	4.93	0.72	265	6
Granodiorite melt		1373 (liquidus)	1388 (wet)–1600 (dry)	2344		0.72	354	6

sharp decrease in the amount of relic clasts that might act as nuclei for heterogeneous nucleation (see later discussion) during the solidification of the melt.

In the case of a thin vein (6 mm), with the same initial T_{melt} of 1450 °C as thick veins, the cooling curve calculated at the vein center nearly overlaps the one calculated at the vein border. This result is consistent with the absence of zoning observed in thin (<6 mm) veins.

6. Discussion

Results from the numerical model show that the origin of zoning in the pseudotachylytes is compatible with cooling of a single pulse of a superheated friction-induced melt inside a host rock at 250 °C. In veins exceeding a critical thickness, zoning develops because (i) different cooling rates are established in the center and in the periphery of the same vein in the temperature range of crystallization, and (ii) different amounts of survivor clasts, acting as (heterogeneous) nucleation sites for microlites/spherulites, are present at different positions in the vein when crystallization starts.

6.1. Thermal vs. microstructural evolution of a thick pseudotachylyte vein

The microstructural evolution of a thick pseudotachylyte vein is summarized below in a 5-time-step sequence matching the thermal evolution calculated in the numerical model (Fig. 10).

Step 1: A clast-laden friction-induced melt with $T_{melt} = 1450$ °C is instantaneously emplaced as a fault vein in a host rock at $T_{hr} = 250$ °C. Injection occurs over a very short time (1–5 s), consistent with the short duration of coseismic slip (e.g. Swanson, 1992). During this step flow structures, including the concentration of clasts at the vein center due to the Bagnold effect (Barrière, 1976), develop in the pseudotachylyte vein.

Step 2: In an initial stage, a dramatic drop of T_{melt} (more than 500 °C in 3–5 s) to values inside the crystallization window of plagioclase occurs at the vein walls; the very high cooling rate likely causes undercooling of the pseudotachylyte melt, which is not taken into account in the model, inhibiting crystallization. However, this effect is counter-acted by heterogeneous nucleation (i.e. growth of crystals on preexisting nuclei; Lofgren, 1983) occurring at both the wall rock and on the surfaces of lithic clasts. The effect of heterogeneous nucleation is to reduce: (i) the degree of undercooling required for nucleation, and (ii) the incubation time for nucleation once the necessary undercooling is attained (Dowty, 1980; Cashman, 1993). Because of the presence of clasts in friction melts (especially near the vein wall where the time of interaction with the melt is short) and the effect of the vein wall, nucleation may occur at cooling rates higher than in experiments with nucleus-free

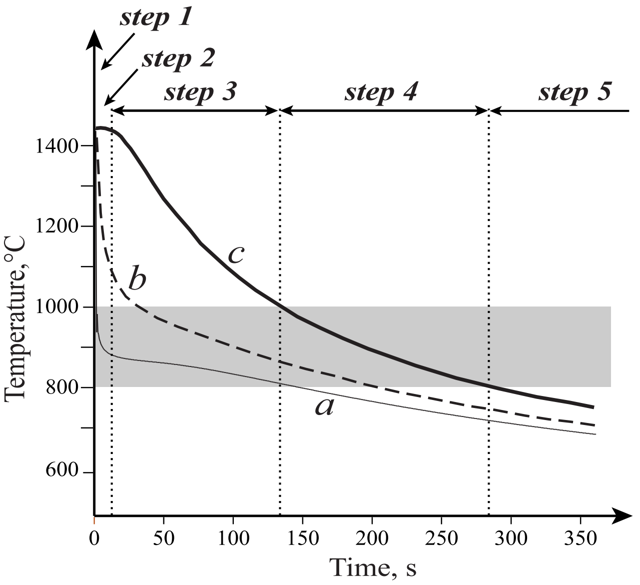

Fig. 10. Cooling curves in a pseudotachylyte fault vein (24 mm thick) calculated at the host rock contact (curve *a*), at a distance of 1.8 mm from the vein wall (curve *b*) and at the vein center (curve *c*). The gray area represents the microlite crystallization interval. Time intervals (steps 1–5) are 'arbitrary' evolutionary steps discussed in the main text. Step 1 (injection of the friction-induced melt) coincides with the ordinate axis.

melts (~0.7 °C s^{-1}; Lesher et al., 1999). Heterogeneous nucleation likely takes place, after the initial stages, when the cooling rate starts to slow down and decreases rapidly to relatively low values. In the rest of the vein, T_{melt} is above the liquidus temperature and partial melting of clasts occurs (Maddock, 1986). In the vein interior, where temperature stays nearly constant at the initial T_{melt}, the rate of consumption of lithic clasts (plagioclase and biotite) is very high, which explains the smaller clast content of the spherulitic domain compared with the microlitic domain. In the spherulitic domain the observed slight decrease in the amount of quartz clasts could indicate some melting of quartz despite the fact that its melting temperature (1726 °C for cristobalite; Navrotsky, 1995) is higher than the friction T_{melt}; this suggests that local equilibrium melting (eutectic melting) may have occurred in cataclasites especially in the finest grained fault rocks.

Step 3: Approximately constant, relatively low cooling rates are set up close to the vein wall during crystallization of plagioclase (and biotite) and inner portions of the veins enter the crystallization window. In the microlitic domain length of plagioclase microlites are up to 100–150 μm in a 24-mm-thick vein (Fig. 4a–c). A microlite length of 150 μm is achieved in 170 s corresponding to an average growth rate of 9×10^{-5} cm s^{-1}; this value is consistent with growth rates estimated in other pseudotachylytes (Petrík et al., 2003) and is about six orders of magnitude higher than those achieved in basaltic lavas lakes at undercooling of 0.01–0.001 °C (growth rate of 5.4×10^{-11}–10^{-10} cm s^{-1} in Cashman (1993)). The very high growth rates of microlites in pseudotachylytes results from the high undercooling associated with the high cooling rates (Petrík et al., 2003). In the microlitic domain cooling rates are relatively low (compared with the spherulitic domain) and become progressively higher away from the vein wall, consistent with crystallization of microlites (as observed in experiments) and their shape evolution from lath to bow-tie/sheaf and finally stellar (Lofgren, 1974). In experiments conducted at cooling rates between 0.5 and 50 °C h^{-1} (=1.4×10^{-4}–1.4×10^{-2} °C s^{-1}), i.e. at cooling rates of 4–2 orders of magnitude smaller than in the study pseudotachylytes, the full range of microlite textures has been produced at a single cooling rate just by varying the nucleation sites (Lofgren, 1983). However, heterogeneous nucleation does not affect the control that cooling rates have on textures for high degrees of undercooling (Lofgren, 1983), which are witnessed, in the study pseudotachylytes, by the very high growth rate of plagioclase microlites. Therefore, in the case of the study pseudotachylytes both heterogeneous nucleation and cooling rates determine the textural variation observed in the microlitic domain. The increase in microlite dimension towards the vein center could be related to the progressive decrease in clast nuclei where partially consumed by melting. Growth of large plagioclase microlites in the transition area between the microlitic domain and the spherulitic domain might explain the development of a 40–100-μm-thick K-feldspar layer observed in some samples (Fig. 4d). The growth of microlites of plagioclase assimilates Ca and Na from the melt leaving a K-enriched layer in this area of the fault vein. In the central part of the vein the T_{melt} is still above the liquidus, when crystallization close to the vein wall is nearly complete, and further assimilation of plagioclase clasts occurs, albeit at reduced rates than in the initial stages after injection. In addition, given the Arrhenius-type dependence of diffusion of chemical species in the melt on temperature, the relatively high cooling rates inhibit migration of elements, released by plagioclase melting, far away from the production site, thus creating Na–Ca-enriched melt haloes surrounding plagioclase relic clasts.

Step 4: After 130–140 s from injection, the T_{melt} in the central part of the vein crosses the temperature of initial crystallization of plagioclase. In the crystallization window, the cooling rate in the vein center is higher than it was at the vein wall (step 3) and spherulites crystallize. Nucleation seeds for plagioclase, especially small clasts, were greatly reduced during the previous clast melt interaction (especially in the very initial stages). Development of plagioclase-nucleus spherulites occurs by heterogeneous nucleation on the few relic plagioclase clasts that remain. Given the complex crystal structure of plagioclase, microlites of plagioclase may require a nucleation substrate that more closely resembles their structure (i.e. plagioclase relic clasts) (Lofgren, 1983). This might explain the absence of microlites surrounding quartz clasts (Fig. 4e). The growth of plagioclase microlites is also favored by the presence of a plagioclase-enriched composition of the melt around the clast related to the slow diffusion rates of chemical species under high cooling rates. Growth of plagioclase microlites might deplete in Ca the nearby surrounding matrix thus explaining the K-rich shell around plagioclase-nucleus spherulites. The combination of relatively high cooling rate, scarcity of nucleation sites and possibly a local change in composition of residual melt may favor undercooling and the persistence of melt across the crystallization window.

Step 5: Below ~800 °C and after ~280 s, plagioclase has crystallized as microlites and spherulites and the K-enriched residual melt inside the spherulitic domain becomes oversaturated in Ti. Microstructures indicate that titanite grains precipitate in a late stage of melt solidification postdating plagioclase in which it is never included. The decrease in grain-size and increase in number of titanite grains may be explained by the progressive increase in cooling rate in progressively inner sections of the vein; this results in an inward decrease of Ti diffusion inhibiting aggregation of titanite nuclei to form a few 'large' titanite grains. Nearly contemporaneous to slightly postdating titanite grain formation is the development of the K-feldspar rims around plagioclase-nucleus spherulites and at the microlitic domain wall. The cryptocrystalline grain-size of the yellow matrix in the spherulitic domain may be related to devitrification of the original pseudotachylyte glass. Experiments on rhyolite glasses at 250 °C and in alkali fluid-rich environments (consistent with the estimated ambient temperatures during pseudotachylyte formation and the K enriched composition of the study fault rocks), give a devitrification rate constant $k_D = 10^{-10}/10^{-12}\ \mathrm{cm}^2\ \mathrm{s}^{-1}$ (Lofgren, 1970). Therefore for a 20-mm-thick zoned fault vein, devitrification of the pseudotachylyte glass may occur in less than one year, given $t = (2a)^2/k_D$. Relatively early devitrification/crystallization of the cryptocrystalline matrix is indicated by the poikilitic character of the epidote rims (Fig. 4f).

A relation between cooling rates and textural zoning also holds in the case of pillow lava and igneous dikes. Pillow lavas show an inverted zoning, compared with zoned fault veins, with glass and spherulites in the outer zone, in contact with water, followed inwards by microlites (McPhie et al., 1993). In contrast with a dike intrusion, where heat is exchanged by conduction, the heat lost by the magma under water involves radiation and convection. Convection currents maintain water in contact with magma at an approximately constant ambient temperature. Under these boundary conditions, numerical modeling of magma cooling indicates higher cooling rates at the pillow surface than in inner portions consistent with the transition from spherulites to microlites towards the pillow core.

Igneous dikes commonly show chilled margins (e.g. Ikeda, 1977), with the cryptocrystalline/glassy domain in a different position than in zoned fault vein. This is well explained by cooling of a non-superheated melt (as in the case of igneous magma: Jaeger, 1968; Philpotts, 1990). Under non-superheated conditions, the melt undercools instantaneously to $T = \alpha T_{\mathrm{melt}} + T_{\mathrm{hr}}$ (with α in the range 0.5–0.65) at the host rock contact (Jaeger, 1968). After this stage, depending on T_{hr} and dike width, temperature may be too low for crystallization and glass is preserved at the dike margins.

6.2. Comparison with the O'Hara's (2001) geothermometer

According to O'Hara (2001), the friction-induced T_{melt} and T_{hr} are related to the clast/matrix ratio (C/M) in pseudotachylyte according to the equation:

$$T_{\mathrm{hr}} = (1 - C/M)T_{\mathrm{melt}} \tag{8}$$

O'Hara's geothermometer is based on thermodynamic considerations and assumes that the mechanical work during fault movement is largely converted to heat along the fault plane to produce friction-induced melts. The T_{melt} of the Lobbia pseudotachylytes, estimated with Eq. (8), are reported in the right column of Table 1 and are in the range of 316–577 °C with a mean value of 379 ± 63 °C. These temperatures are considerably lower than those inferred from the crystallization of An_{40} plagioclase microlites (1000–1080 °C from Lesher et al. (1999)) and are not consistent with the development of the textural zoning of the zoned fault veins, which is suggested to require superheated melts ($T_{\mathrm{melt}} \cong 1450$ °C). The inconsistency between the different temperature estimates is possibly explained by the presence of the cataclastic precursor to pseudotachylyte.

In the case of the GGFZ, there is field and microstructural evidence that pseudotachylytes are commonly preceded by development of cataclasites/ultracataclasites. Kinematic indicators from both cataclasites and pseudotachylytes indicate the same sense of shear, but there is not a clear indication whether the different fault rocks represent incremental deformation products at different stages of a continuous short-lived co-seismic episode (a 'single-jerk' episode) or if they resulted from separate slip episodes along the fault. In the former case the energy budgets 'spent' along the fault are cumulative and most of the mechanical work is converted to heat, as assumed in O'Hara's model. This is probably the case for pseudotachylytes generated during landslides (Lin et al., 2001), where abrasive wear and frictional melting occur during a single-jerk event and, therefore, O'Hara's geothermometer can be used. In this case, the volume of glass may be estimated from diffraction data (Lin et al., 2001) and Eq. (8) yields $T_{\mathrm{melt}} \sim 1400$ °C; this value is consistent with values of T_{melt} estimated from glass composition and with the observation that survivor clasts in pseudotachylytes are mostly quartz.

In the case of the study pseudotachylytes, the discrepancy between the T_{melt} inferred from the numerical model and those estimated by O'Hara's geothermometer may reflect a more complex slip history than a single coseismic slip event along the fault. On the other hand, strong fluid–rock interaction synkinematic to cataclasites is well documented in the studied rocks by diffuse alteration haloes around fault zones, widespread veining and compositional changes of cataclasites compared with undeformed host rocks (Table 3). These phenomena must have altered, at least locally, the mechanical properties of fault material by inducing partial to complete induration of cataclasites before production of pseudotachylytes (which commonly include cataclasite clasts) (Di Toro, 2003). This is clearly inconsistent with seismogenic single-jerk movement on a fault.

It is proposed that O'Hara geothermometer may be used in combination with independent estimates of the friction T_{melt} as an indicator of the deformation history along a fault. Differences between T_{melt} evaluated with Eq. (8) and those from other methods may indicate that the deformation path deviates from that of a single coseismic slip event on a fault surface.

7. Conclusions

The Gole Larghe–Val di Genova Fault Zone is a dextral strike-slip fault cutting across the northern Adamello batholith. The fault zone is outlined by an association of synkinematic indurated cataclasites and pseudotachylytes, which developed under ambient temperature and pressure conditions of ~250–300 °C and 0.25–0.3 GPa, respectively. Relatively thick (>6 mm) pseudotachylytes veins are zoned with two symmetric microlitic domains sandwiching an inner spherulitic layer. The thickness of both domains increases linearly with total vein thickness.

The microlitic and spherulitic domains exhibit a complex succession of textures, possibly related to differences in cooling rate across the vein during solidification of the friction-induced melt. This relationship between texture and cooling rates may be used to infer the initial T_{melt}. It may be tempting to use directly crystal morphologies as a geothermometer, but as Lofgren (1974, 1980, 1983) states, many parameters control the diffusion rate and affect the morphology of a crystal during crystallization, such as water content, O_2 fugacity, melt composition, and density of nuclei.

Using a numerical model we correlate the texture of zoned fault vein to the contrasting cooling rates at different positions within the fault vein. The observed microstructures are compatible with the injection of a superheated friction-induced melt having a starting $T_{melt} \cong 1450$ °C in a host rock at $T = 250–300$ °C. In contrast, temperature estimates based on the geothermometer of O'Hara (2001) yield $T_{melt} < 577$ °C for the same pseudotachylytes. The inconsistency between the two T_{melt} estimates can be explained by the composite deformational history of precursor cataclasites, since O'Hara's geothermometer assumes that clast fragmentation and frictional melting occur during the same seismic event. The disagreement between two T_{melt} estimates using different methods might give an insight into the fault processes responsible for the association of cataclasites and pseudotachylytes.

Acknowledgements

The authors thanks Luca Peruzzo and Richard Spiess (SEM facilities), Raul Carampin (electron microprobe), Daria Pasqual (XRF), William Collins and Richard Yund (TEM samples preparation), Antonio Novello (thin sections) and Giancarlo Narduzzo (technical support). The reviews by Mark Swanson and Kirean O'Hara are greatly acknowledged. Bernardo Cesare, Jan Tullis, Holger Stünitz, Michael Stipp and Judith Chester are also acknowledged for insightful discussions and David Goldsby for an invaluable pre-review of the paper. The Provincia Autonoma di Trento provided logistic support during the field study. Image analysis was performed using the public domain NIH image program (developed at the US National Institutes of Health and available on the Internet at http://rsb/info.nih.gov/nih-image/). This work has been funded by a MURST Italian Grant: Progetto 248 Giovani Ricercatori Anno 2000.

References

Austrheim, H., Boundy, T.M., 1994. Pseudotachylytes generated during seismic faulting and eclogitization of the deep crust. Science 265, 82–83.

Barrière, M., 1976. Flowage differentiation: limitation of the Bagnold effect to the narrow intrusions. Contribution to Mineralogy and Petrology 55, 139–145.

Berlenbach, J.W., Roering, C., 1992. Sheath-fold-like structures in pseudotachylyte. Journal of Structural Geology 14, 847–856.

Bianchi, A., Callegari, E., Jobstraibizer, P.G., 1970. I tipi petrografici fondamentali del plutone dell'Adamello. Memorie degli Istituti di Geologia e Mineralogia dell'Università di Padova 27, 1–148.

Burnham, C.W., 1979. The importance of volatile constituents. In: Yoder, H.S., (Ed.), The Evolution of Igneous Rocks, Princeton University Press, Princeton, pp. 439–474.

Camacho, A., Vernon, R.H., Fitz Gerald, J.D., 1995. Large volumes of anhydrous pseudotachylyte in the Woodroffe Thrust, eastern Musgrave Ranges, Australia. Journal of Structural Geology 17, 371–383.

Carslaw, H.S., Jaeger, J.C., 1959. Conduction of Heat in Solids, 2nd edition, Oxford at the Clarendon Press, Oxford.

Cashman, K.V., 1993. Relationships between plagioclase crystallization and cooling rate in basaltic melts. Contributions to Mineralogy and Petrology 113, 126–142.

Clauser, C., Huenges, E., 1995. Thermal conductivity of rocks and minerals. In: Aherens, J.T. (Ed.), Rock Physics and Phase Relations. A Handbook of Physical Constants. AGU Reference Shelf 3, pp. 105–126.

Crank, J., Nicholson, P., 1947. A practical method for numerical evaluation of solutions of partial differential equations of heat-conduction type. Proceedings of the Cambridge Philosophical Society 43, 50–67.

Deer, W.A., Howie, R.A., Zussman, J., 1992. An Introduction to the Rock-Forming Minerals, Longman, Harlow, Essex, England.

Del Moro, A., Pardini, G., Quercioli, C., Villa, I., Callegari, E., 1983. Rb/Sr and K/Ar chronology of Adamello granitoids, Southern Alp. Memorie Società Geologica Italiana 26, 285–299.

Di Toro, G., 2003. Processes on fault surfaces of seismic shear zones. Ph.D. thesis, University of Padova.

Dowty, E., 1980. Crystal growth and nucleation theory and numerical simulation of igneous crystallization. In: Hargraves, R.B., (Ed.), Physics of Magmatic Processes, Princeton University Press, Princeton, pp. 419–485.

Fabbri, O., Lin, A., Tokushige, H., 2000. Coeval formation of cataclasite and pseudotachylyte in a Miocene forearc granodiorite, southern Kyushu, Japan. Journal of Structural Geology 22, 1015–1025.

Fourier, J.B., 1822. Theorie analytique de la chaleur. Reproduction for C.H. Hall, Breslau, Koebner, 1883.

Grocott, J., 1981. Fracture geometry of pseudotachylyte generation zones: a study of shear fractures formed during seismic events. Journal of Structural Geology 3, 169–178.

Guilbert, J.M., Park, C.F., 1986. The Geology of Ore Deposits, Freeman and Company, New York.

Holland, T.B., Powell, R., 1990. An enlarged and updated internally consistent thermodynamic dataset with uncertainties and correlations: the system K_2O–Na_2O–CaO–MgO–MnO–FeO–Fe_2O_3–Al_2O_3–TiO_2–SiO_2–C–H_2–O_2. Journal of Metamorphic Geology 8, 89–124.

Ikeda, Y., 1977. Grain size of plagioclase of the basaltic andesitic dikes, Iritono, central Abukuma plateau. Canadian Journal of Earth Sciences 14, 1860–1866.

Jaeger, J.C., 1968. Cooling and solidification of igneous rocks. In: Hess, H.H., Poldevaart, A. (Eds.), Basalts, Vol. 2. Interscience Publishers, New York, pp. 503–536.

Killick, A.M., Roering, C., 1998. An estimate of the physical conditions of pseudotachylite formation in the West Rand Goldfield, Witwatersrand Basin, RSA. Tectonophysics 284, 247–259.

Lesher, C.E., Cashman, K.V., Mayfield, J.D., 1999. Kinetic controls on crystallization of Tertiary North Atlantic basalt and implications for the emplacement and cooling history of lava at Site 989, Southeast Greenland rifted margin. In: Larsen, H.C., Duncan, R.A., Allan, J.F., Brooks, K. (Eds.), Proceeding of the ODP, Scientific Results, 163, College Station, Texas (Ocean Drilling Program), pp. 3–16.

Lin, A., 1994a. Glassy pseudotachylytes from the Fuyun Fault Zone, Northwest China. Journal of Structural Geology 16, 71–83.

Lin, A., 1994b. Microlite morphology and chemistry in pseudotachylyte, from the Fuyun Fault Zone, Northwest China. Journal of Geology 102, 317–329.

Lin, A., Shimamoto, T., 1998. Selective melting processes as inferred from experimentally generated pseudotachylytes. Journal of Asian Earth Sciences 16, 533–545.

Lin, A., Chen, A., Liau, C., Lee, C., Lin, C., Lin, P., Wen, S., Ouchi, T., 2001. Frictional fusion due to coseismic slip landsliding during the 1999 Chi-Chi (Taiwan) ML 7.3 earthquake. Geophysical Research Letters 28, 4011–4014.

Lofgren, G., 1970. Experimental devitrification rate of rhyolitic glass. Geological Society of America Bulletin 81, 553–560.

Lofgren, G., 1971. Spherulitic textures in glassy and crystalline rocks. Journal of Geophysical Research 76, 5635–5648.

Lofgren, G., 1974. An experimental study of plagioclase crystal morphology: isothermal crystallization. American Journal of Science 274, 243–273.

Lofgren, G., 1980. Experimental studies on the dynamic crystallization of silicate melts. In: Hargraves, R.B., (Ed.), Physics of Magmatic Processes, Princeton University Press, Princeton, pp. 487–551.

Lofgren, G., 1983. Effect of heterogeneous nucleation on basaltic textures: a dynamic crystallization study. Journal of Petrology 24, 229–255.

Macaudière, J., Brown, L.W., Ohnenstetter, D., 1985. Microcrystalline textures resulting from rapid crystallization in a pseudotachylite melt in a meta-anorthosite. Contribution to Mineralogy and Petrology 89, 39–51.

Maddock, R.H., 1983. Melt origin of fault-generated pseudotachylytes demonstrated by textures. Geology 11, 105–108.

Maddock, R.H., 1986. Partial melting of lithic porphyroclasts in fault-generated pseudotachylytes. Neues Jahrbuch für Mineralogie—Abhandlungen 155, 1–14.

Maddock, R.H., Grocott, J., Van Nes, M., 1987. Vesicles, amygdales and similar structures in fault-generated pseudotachylytes. Lithos 20, 419–432.

Magloughlin, J.F., 1998. Amygdales within pseudotachylyte. In: Snoke, A.W., Tullis, J., Todd, V.R. (Eds.), Fault Related Rocks—A Photographic Atlas, Princeton, New Jersey, pp. 88–89.

Magloughlin, J.F., Spray, J.G., 1992. Frictional melting processes and products in geological materials: introduction and discussion. Tectonophysics 204, 197–206.

Marsh, B.D., 2000. Magma chambers. In: Sigurdsson, H., (Ed.), Encyclopedia of Volcanoes, Academic Press, San Diego, pp. 191–217.

McPhie, J., Doyle, M., Allen, R., 1993. Volcanic Textures: a Guide to the Interpretation of Textures in Volcanic Rocks, Centre for Ore Deposit and Exploration Studies, University of Tasmania, 198pp.

Müller, W., Kelley, S.P., Villa, I.M., 2002. Dating fault-generated pseudotachylytes: comparison of $^{40}Ar/^{39}Ar$ stepwise-heating, laser-ablation and Rb–Sr microsampling analyses. Contribution of Mineralogy and Petrology 144, 57–77.

Navrotsky, A., 1995. Thermodynamic properties of minerals. In: Rock Physics and Phase Relations. A Handbook of Physical Constants. AGU Reference Shelf 2, pp. 18–32.

O'Hara, K., 2001. A pseudotachylyte geothermometer. Journal of Structural Geology 23, 1345–1357.

O'Hara, K., Sharp, Z.D., 2001. Chemical and oxygen isotope composition of natural and artificial pseudotachylyte: role of water during frictional melting. Earth and Planetary Science Letters 184, 393–406.

Petrík, I., Nabalek, I.P., Janàk, M., PlaŤienka, D., 2003. Conditions of formation and crystallization kinetics of highly oxidized pseudotachylytes form the High Tatras (Slovakia). Journal of Petrology 44, 901–927.

Philpotts, A.R., 1990. Principles of Igneous and Metamorphic Petrology, Prentice Hall, Englewood Cliffs.

Ray, S.K., 1999. Transformation of cataclastically deformed rocks to pseudotachylyte by pervasion of frictional melt: inferences from clast size analysis. Tectonophysics 301, 283–304.

Scholz, C.H., 1990. The Mechanics of Earthquakes and Faulting, Cambridge Press, New York.

Shimada, K., Kobari, Y., Okamoto, T., Takagi, H., Saka, Y., 2001. Pseudotachylyte veins associated with granitic cataclasite along the Median Tectonic Line, eastern Kii Peninsula, Southwest Japan. The Journal of the Geological Society of Japan 107, 117–128.

Sibson, R.H., 1975. Generation of pseudotachylyte by Ancient Seismic Faulting. Geophysical Journal of Royal Astronomical Society 43, 775–794.

Spear, F.K., 1995. Metamorphic Phase Equilibria and Pressure–Temperature–Time Paths, 2nd Printing, Mineralogical Society of America, Washington.

Spera, F.K., 2000. Physical properties of magmas. In: Sigurdsson, H., (Ed.), Encyclopedia of Volcanoes, Academic Press, San Diego, pp. 171–190.

Spray, J.G., 1992. A physical basis for the frictional melting of some rock forming minerals. Tectonophysics 204, 205–221.

Spray, J.G., 1995. Pseudotachylyte controversy: fact or friction? Geology 23, 1119–1122.

Stipp, M., Stünitz, H., Heilbronner, R., Schmid, S., 2002. The eastern Tonale fault zone: a 'natural laboratory' for crystal plastic deformation of quartz over a temperature range from 250 to 700 °C. Journal of Structural Geology 24, 1861–1884.

Swanson, M.T., 1989. Side wall ripouts in strike-slip faults. Journal of Structural Geology 11, 933–948.

Swanson, M.T., 1992. Fault structure, wear mechanisms and rupture processes in pseudotachylyte generation. Tectonophysics 204, 223–242.

Toyoshima, T., 1990. Pseudotachylite from the Main Zone of the Hidaka metamorphic belt. Hokkaido, northern Japan. Journal of Metamorphic Geology 8, 507–523.

Viola, G., 2000. Kinematics and timing of the Periadriatic fault system in the Giudicarie region (Central Eastern-Alps). Ph.D. thesis, ETH Zurich.

Warr, L.N., van der Pluijum, B.A., Peacor, D.R., Hall, C.M., 2003. Frictional melt pulses during a ~1.1 Ma earthquake along the Alpine Fault, New Zealand. Earth and Planetary Science Letters 209, 39–52.

Watson, E.B., Brenan, J.M., 1987. Fluids in the lithosphere. 1. Experimentally-determined wetting characteristics of CO_2–H_2O fluids and their implications for fluid transport, host-rock physical properties, and fluid inclusion formation. Earth and Planetary Science Letters 85, 497–515.

Wenk, H.R., Johnson, L.R., Ratschbacher, L., 2000. Pseudotachylites in the Eastern Peninsular Ranges of California. Tectonophysics 321, 253–277.

Werling, E., 1992. Tonale-, Pejo- und Judicarien-Linie: Kinematic, Mikrostrukturen und Metamorphose von Tektoniken aus raumlich interferierenden aber verschiedenaltrigen Verwerfungszonen. PhD. thesis, ETH Zurich.